Supplementary Materials

High-speed image reconstruction for optically sectioned, super-resolution structured illumination microscopy

Zhaojun Wang[a], Tianyu Zhao[a], Huiwen Hao[b], Yanan Cai[c], Kun Feng[a], Xue Yun[a], Yansheng Liang[a], Shaowei Wang[a], Yujie Sun[b], Piero R. Bianco[d], Kwangsung Oh[e], and Ming Lei[a,*]

[a] MOE Key Laboratory for Nonequilibrium Synthesis and Modulation of Condensed Matter, Shaanxi Province Key Laboratory of Quantum Information and Quantum Optoelectronic Devices, School of Physics, Xi'an Jiaotong University, Xi'an 710049, China
[b] State Key Laboratory of Membrane Biology & Biomedical Pioneer Innovation Center (BIOPIC) & School of Life Sciences, Peking University, Beijing 100871, China
[c] College of Science, Northwest A&F University, Yangling 712100, China
[d] Department of Pharmaceutical Sciences, College of Pharmacy, University of Nebraska Medical Center, Omaha, NE 68198-6025, USA
[e] Department of Computer Science, College of Information Science & Technology, University of Nebraska Omaha, Omaha, NE 68182, USA

*Correspondence Author, E-mail: ming.lei@mail.xjtu.edu.cn

Supplementary Note 1: General form of the reconstruction algorithm in real space and its relationship to the conventional workflow in the Fourier Domain

The origin of the concept to reconstruct the SR image in real space dates back to the earliest work of Lukosz[20] in the 1960s, which appeared as an early thought of SR-SIM. In 2001, So et al.[21] comprehensively interpreted the principle of SR-SIM in the spatial domain and gave the explicit expression of the spatial domain interpretation of SR-SIM. However, this interpretation was not further exploited as a reconstruction algorithm. In 2008, Somekh et al.[22] established a new reconstruction method to facilitate quantitative noise analysis of SR-SIM, which yielded the SR image from the raw SIM images without the need to perform Fourier transforms. This was the first time that spatial domain interpretation appeared as a reconstruction method. Since then, no new progress on spatial domain processing was reported. Till 2021, we further exploited it a rapid reconstruction algorithm[23] termed spatial domain reconstruction algorithm. This resulted in a heated discussion about spatial domain processing[48,49]. In our previous work, the spatial domain reconstruction algorithm was shown to be 7-fold faster than conventional Wiener-SIM. However, its phase shifts are limited to a specific value (0, 2π/3, 4π/3), and its relationship with the conventional frequency-domain reconstruction algorithm was not distinctly deduced, which may prohibit its widespread application in SR-SIM communities. In this note, we further present a general form of the algorithm and clarify the relation of this method with the conventional reconstruction algorithm implemented in the Fourier domain.

1.1 Deduction of the general form of the reconstruction algorithm in real space

For linear structured illumination microscopy, the detected intensity distribution at the sensor plane can be described by the following equation

$$D(\boldsymbol{r}) = [O(\boldsymbol{r}) \cdot I(\boldsymbol{r})] \otimes H(\boldsymbol{r}) \tag{1}$$

where $O(\boldsymbol{r})$ denotes the spatial distribution of fluorophore in the labeled specimen, $I(\boldsymbol{r})$ represents the intensity distribution of the excitation field, and $H(\boldsymbol{r})$ depicts the point spread function of the microscope. The symbol $\otimes$ represents the convolution operation. By shifting the excitation field with a lateral movement, the above equation can be revised as

$$D_i(\boldsymbol{r}) = [O(\boldsymbol{r}) \cdot I(\boldsymbol{r} - \boldsymbol{r}_i')] \otimes H(\boldsymbol{r}) \tag{2}$$

where $\boldsymbol{r}_i'$ denotes the lateral shift of the field. Without loss of generality, we only consider the structured light field in one dimension. Therefore, the vector $\boldsymbol{r}$ can be replaced by a scalar x:

$$D_i(x) = \int O(x'') I(x'' - x_i') H(x - x'') dx'' \tag{3}$$

For fringe patterns, the illumination field can be described by a cosine function:

$$I(x) = I_0[1 + m\cos(\omega x + \varphi_0)] \tag{4}$$

where I_0, m, ω, φ_0 denote the average intensity, the modulation depth, the angular frequency, and the initial phase of the illumination field, respectively.

Assuming there exists $c_1(x)$, $c_2(x)$, and $c_3(x)$ that makes the following equation always true for any $O(x)$ and $H(x)$, the effective PSF of the system can be obtained by multiplying the wide-field PSF with a modulation function $1 + \cos(\omega x)$:

$$I_{\text{SR-SIM}}(x) = c_1(x)D_1(x) + c_2(x)D_2(x) + c_3(x)D_1(x) = O(x) \otimes \{[1 + \cos(\omega x)] \cdot H(x)\} \tag{5}$$

As a result, the FWHM of the effective PSF turns out to be half that of wide-field PSF, with which the super-resolution image can be directly obtained. Then, how to get the $c_1(x)$、$c_2(x)$、$c_3(x)$ is the key procedure of the above hypothesis.

By substituting Eq. 2 and Eq. 3 into the above formula, the precondition for the establishment of Eq.5 can be simplified as

$$I_0 \sum_{i=1}^{3} c_i(x)[1 + m\cos(\omega x'' + \varphi_0 - \omega x_i')] = 1 + \cos(\omega x - \omega x'')$$

$$= 1 + \cos[(\omega x + \varphi_0) - (\omega x'' + \varphi_0)]$$

(6)

By rewriting both sides of this equation as a function of $\cos(\omega x'' + \varphi_0)$ and $\sin(\omega x'' + \varphi_0)$, above equation can be transformed into

$$I_0 \sum_{i=1}^{3} c_i(x) + [mI_0 \sum_{i=1}^{3} c_i(x)\cos(\omega x_i')]\cos(\omega x'' + \varphi_0) + [mI_0 \sum_{i=1}^{3} c_i(x)\sin(\omega x'' + \varphi_0)]\sin(\omega x_i')$$

$$= 1 + \cos(\omega x + \varphi_0)\cos(\omega x'' + \varphi_0) + \sin(\omega x + \varphi_0)\sin(\omega x'' + \varphi_0)$$

(7)

According to the orthogonality of $\cos(\omega x'' + \varphi_0)$ and $\sin(\omega x'' + \varphi_0)$, $c_1(x)$, $c_2(x)$, $c_3(x)$ must satisfy the following relations if we want the above formula to be constant for any x and x'':

$$\sum_{i=1}^{3} c_i(x) = \frac{1}{I_0}$$

(8)

$$\sum_{i=1}^{3} c_i(x)\cos(\omega x_i') = \frac{1}{mI_0}\cos(\omega x + \varphi_0)$$

(9)

$$\sum_{i=1}^{3} c_i(x)\sin(\omega x_i') = \frac{1}{mI_0}\sin(\omega x + \varphi_0)$$

(10)

Assuming the phase shift to be $\omega x_i' \in \{0, \Delta\varphi_1, \Delta\varphi_2\}$, above relations can be expressed as follow:

$$\begin{pmatrix} 1 & 1 & 1 \\ 1 & \cos\Delta\varphi_1 & \cos\Delta\varphi_2 \\ 0 & \sin\Delta\varphi_1 & \sin\Delta\varphi_2 \end{pmatrix} \begin{pmatrix} c_1(x) \\ c_2(x) \\ c_3(x) \end{pmatrix} = \begin{pmatrix} \dfrac{1}{I_0} \\ \dfrac{1}{mI_0}\cos(\omega x + \varphi_0) \\ \dfrac{1}{mI_0}\sin(\omega x + \varphi_0) \end{pmatrix}$$

(11)

Let

4

$$\mathbf{S} = \begin{pmatrix} 1 & 1 & 1 \\ 1 & \cos\Delta\varphi_1 & \cos\Delta\varphi_2 \\ 0 & \sin\Delta\varphi_1 & \sin\Delta\varphi_2 \end{pmatrix} \tag{12}$$

As long as the phase shift satisfies $|\mathbf{S}| \triangleq \sin(\Delta\varphi_2 - \Delta\varphi_1) + \sin\Delta\varphi_1 - \sin\Delta\varphi_2 \neq 0$, $c_1(x)$、 $c_2(x)$、

$c_3(x)$ always can be solved as

$$
\begin{aligned}
\begin{pmatrix} c_1(x) \\ c_2(x) \\ c_3(x) \end{pmatrix} &= \begin{pmatrix} 1 & 1 & 1 \\ 1 & \cos\Delta\varphi_1 & \cos\Delta\varphi_2 \\ 0 & \sin\Delta\varphi_1 & \sin\Delta\varphi_2 \end{pmatrix}^{-1} \begin{pmatrix} \dfrac{1}{I_0} \\ \dfrac{1}{mI_0}\cos(\omega x + \varphi_0) \\ \dfrac{1}{mI_0}\sin(\omega x + \varphi_0) \end{pmatrix} \\[2mm]
&= \frac{1}{|S|} \begin{pmatrix} \sin(\Delta\varphi_2 - \Delta\varphi_1) & \sin\Delta\varphi_1 - \sin\Delta\varphi_2 & \cos\Delta\varphi_2 - \cos\Delta\varphi_1 \\ -\sin\Delta\varphi_2 & \sin\Delta\varphi_2 & 1 - \cos\Delta\varphi_2 \\ \sin\Delta\varphi_1 & -\sin\Delta\varphi_1 & \cos\Delta\varphi_1 - 1 \end{pmatrix} \begin{pmatrix} \dfrac{1}{I_0} \\ \dfrac{1}{mI_0}\cos(\omega x + \varphi_0) \\ \dfrac{1}{mI_0}\sin(\omega x + \varphi_0) \end{pmatrix}
\end{aligned} \tag{13}
$$

The above formulas are the general expressions of $c_1(x)$、 $c_2(x)$、 $c_3(x)$. Specifically, when

the phase shifts are set as $\{0, \alpha, 2\alpha\}$, the formulas can be simplified to:

$$
\begin{pmatrix} c_1(x) \\ c_2(x) \\ c_3(x) \end{pmatrix} = \begin{pmatrix} \dfrac{1}{2(1-\cos\alpha)} & \dfrac{1-2\cos\alpha}{2(1-\cos\alpha)} & -\dfrac{2\cos\alpha+1}{2\sin\alpha} \\[2mm] -\dfrac{\cos\alpha}{1-\cos\alpha} & \dfrac{\cos\alpha}{1-\cos\alpha} & \dfrac{1+\cos\alpha}{\sin\alpha} \\[2mm] \dfrac{1}{2(1-\cos\alpha)} & -\dfrac{1}{2(1-\cos\alpha)} & -\dfrac{1}{2\sin\alpha} \end{pmatrix} \begin{pmatrix} \dfrac{1}{I_0} \\ \dfrac{1}{mI_0}\cos(\omega x + \varphi_0) \\ \dfrac{1}{mI_0}\sin(\omega x + \varphi_0) \end{pmatrix} \tag{14}
$$

More specifically, if we limit the phase shift as $\{0, 2\pi/3, 4\pi/3\}$, the expressions of $c_1(x)$、

$c_2(x)$、 $c_3(x)$ can be further simplified to the equation below:

5

$$\begin{pmatrix} c_1(x) \\ c_2(x) \\ c_3(x) \end{pmatrix} = \begin{pmatrix} \dfrac{1}{3} & \dfrac{2}{3} & 0 \\[2mm] \dfrac{1}{3} & -\dfrac{1}{3} & \dfrac{\sqrt{3}}{3} \\[2mm] \dfrac{1}{3} & -\dfrac{1}{3} & -\dfrac{\sqrt{3}}{3} \end{pmatrix} \begin{pmatrix} \dfrac{1}{I_0} \\[2mm] \dfrac{1}{mI_0}\cos(\omega x + \varphi_0) \\[2mm] \dfrac{1}{mI_0}\sin(\omega x + \varphi_0) \end{pmatrix} = \begin{pmatrix} \dfrac{1}{3I_0}[1+\dfrac{2}{m}\cos(\omega x + \varphi_0)] \\[2mm] \dfrac{1}{3I_0}[1+\dfrac{2}{m}\cos(\omega x + \varphi_0 - \dfrac{2\pi}{3})] \\[2mm] \dfrac{1}{3I_0}[1+\dfrac{2}{m}\cos(\omega x + \varphi_0 + \dfrac{2\pi}{3})] \end{pmatrix} \qquad (15)$$

which is identical to the result provided in Ref. [23].

The coefficient functions $c_i(x)$ are fully determined by the illumination parameters (initial phase, pattern frequency, phase shifts, and the modulation depth), which is however invariant with the distribution of the specimen. Therefore, after the illumination parameters are determined, the coefficients can be precalculated and be reused for continuous reconstructions. As long as the illumination parameters do not change, a super-resolution image without deconvolution can be directly obtained by multiplying the raw images with these coefficient functions and superimposing the products, as described in Eq. (5), thus greatly reducing the execution time of the reconstruction.

1.2 Demonstration of the relationship of the reconstruction algorithm in real space and the conventional reconstruction approach in Fourier domain

The 3×3 matrix on the right side of Eq. (13) is determined by the phase shifts of the fringes, which remain constant during calculation. Denoting the elements of the matrix as $C_{p,q}$ (p=1,2,3; q=1,2,3), the equation can be converted to

$$\begin{pmatrix} c_1(x) \\ c_2(x) \\ c_3(x) \end{pmatrix} = \begin{pmatrix} C_{11} & C_{12} & C_{13} \\ C_{21} & C_{22} & C_{23} \\ C_{31} & C_{32} & C_{33} \end{pmatrix} \begin{pmatrix} \dfrac{1}{I_0} \\[2mm] \dfrac{1}{mI_0}\cos(\omega x + \varphi_0) \\[2mm] \dfrac{1}{mI_0}\sin(\omega x + \varphi_0) \end{pmatrix} \qquad (16)$$

where the coefficient matrix can be calculated as follow

$$\begin{pmatrix} C_{11} & C_{12} & C_{13} \\ C_{21} & C_{22} & C_{23} \\ C_{31} & C_{32} & C_{33} \end{pmatrix} = \frac{1}{|S|} \begin{pmatrix} \sin(\Delta\varphi_2 - \Delta\varphi_1) & \sin\Delta\varphi_1 - \sin\Delta\varphi_2 & \cos\Delta\varphi_2 - \cos\Delta\varphi_1 \\ -\sin\Delta\varphi_2 & \sin\Delta\varphi_2 & 1 - \cos\Delta\varphi_2 \\ \sin\Delta\varphi_1 & -\sin\Delta\varphi_1 & \cos\Delta\varphi_1 - 1 \end{pmatrix} \tag{17}$$

As such, the super-resolution image can be transformed to the following expression

$$\begin{aligned} D_{SR}(x) &= c_1(x)D_1(x) + c_2(x)D_2(x) + c_3(x)D_1(x) \\ &= \frac{1}{I_0}[C_{11}D_1(x) + C_{21}D_2(x) + C_{31}D_3(x)] \\ &\quad + \frac{1}{mI_0}[C_{12}D_1(x) + C_{22}D_2(x) + C_{32}D_3(x)]\cos(\omega x + \varphi_0) \\ &\quad + \frac{1}{mI_0}[C_{13}D_1(x) + C_{23}D_2(x) + C_{33}D_3(x)]\sin(\omega x + \varphi_0) \end{aligned} \tag{18}$$

To reveal the relation between spatial and frequency domain reconstruction, we introduce three intermediate images $R_0(x)$、$R_1(x)$、$R_2(x)$ as below

$$\begin{aligned} R_0(x) &= \frac{1}{I_0}[C_{11}D_1(x) + C_{21}D_2(x) + C_{31}D_3(x)] \\ R_1(x) &= \frac{1}{mI_0}[C_{12}D_1(x) + C_{22}D_2(x) + C_{32}D_3(x)] \\ R_2(x) &= \frac{1}{mI_0}[C_{13}D_1(x) + C_{23}D_2(x) + C_{33}D_3(x)] \end{aligned} \tag{19}$$

which are linear combinations of the three raw images $D_1(x)$、$D_2(x)$、$D_3(x)$, and the combination coefficients are completely determined by the illumination parameters. Then, the super-resolution image can be rewritten as

$$I_{SR\text{-}SIM}(x) = R_0(x) + R_1(x)\cos(\omega x + \varphi_0) + R_2(x)\sin(\omega x + \varphi_0) \tag{20}$$

In other words, the super-resolution image without deconvolution in Eq. (5) can be obtained in another way: first calculate $R_0(x)$、$R_1(x)$、$R_2(x)$ with Eq.(19); then multiply $R_0(x)$、$R_1(x)$、

$R_2(x)$ respectively with 1, $\cos(\omega x + \varphi_0)$, $\sin(\omega x + \varphi_0)$ and finally add the products together. This new reconstruction workflow implemented in real space provides insight into the connection of the reconstruction algorithm in real space and the conventional workflow in the Fourier Domain.

By substituting the expressions of the coefficients in Eq. (17) into Eq. (19) and expressing $D_1(x)$、$D_2(x)$、$D_3(x)$ as the convolution form shown in Eq. (2) (without loss of generality, let $I_0=1$), $R_0(x)$、$R_1(x)$、$R_2(x)$ can be derived to the following form

$$
\begin{aligned}
R_0(x) &= O(x) \otimes H(x) = \tilde{S}_0(k) \\
R_1(x) &= [O(x)\bullet\cos(\omega x + \varphi_0)] \otimes H(x) \\
R_2(x) &= [O(x)\bullet\sin(\omega x + \varphi_0)] \otimes H(x)
\end{aligned}
\tag{21}
$$

in which $R_0(x)$ is the zero-order component of the specimen. Further, $R_1(x)$、$R_2(x)$ can be derived as follow

$$
\begin{aligned}
R_1(x) &= [O(x)\bullet\cos(\omega x + \varphi_0)] \otimes H(x) \\
&= [O(x)\bullet\frac{e^{i(\omega x+\varphi_0)} + e^{-i(\omega x+\varphi_0)}}{2}] \otimes H(x) \\
&= \frac{e^{i\varphi_0}}{2}[O(x)\bullet e^{i\omega x}] \otimes H(x) + \frac{e^{-i\varphi_0}}{2}[O(x)\bullet e^{-i\omega x}] \otimes H(x) \\
&= \frac{e^{i\varphi_0}}{2}\mathcal{F}^{-1}[\tilde{O}(k-\omega)\bullet\tilde{H}(k)] + \frac{e^{-i\varphi_0}}{2}\mathcal{F}^{-1}[\tilde{O}(k+\omega)\bullet\tilde{H}(k)] \\
R_2(x) &= [O(x)\bullet\sin(\omega x + \varphi_0)] \otimes H(x) \\
&= [O(x)\bullet\frac{e^{i(\omega x+\varphi_0)} - e^{-i(\omega x+\varphi_0)}}{2i}] \otimes H(x) \\
&= \frac{e^{i\varphi_0}}{2i}[O(x)\bullet e^{i\omega x}] \otimes H(x) - \frac{e^{-i\varphi_0}}{2i}[O(x)\bullet e^{-i\omega x}] \otimes H(x) \\
&= \frac{e^{i\varphi_0}}{2i}\mathcal{F}^{-1}[\tilde{O}(k-\omega)\bullet\tilde{H}(k)] - \frac{e^{-i\varphi_0}}{2i}\mathcal{F}^{-1}[\tilde{O}(k+\omega)\bullet\tilde{H}(k)]
\end{aligned}
\tag{22}
$$

Therefore, the super-resolution spectra in the conventional frequency-domain reconstruction can be represented by

$$\tilde{O}(k-\omega)\bullet\tilde{H}(k)=\mathrm{e}^{-i\varphi_0}\mathcal{F}[R_1(x)+iR_2(x)]$$
$$\tilde{O}(k+\omega)\bullet\tilde{H}(k)=\mathrm{e}^{i\varphi_0}\mathcal{F}[R_1(x)-iR_2(x)]$$

(23)

By shifting them back to their original position, the first-order components can be derived

as

$$
\begin{aligned}
\tilde{S}_{-1}(k)=\tilde{O}(k)\bullet\tilde{H}(k-\omega)&=\mathcal{F}\left\{\mathcal{F}^{-1}\left[\tilde{O}(k+\omega)\bullet\tilde{H}(k)\right]\mathrm{e}^{i\omega x}\right\}\\
&=\mathcal{F}\left\{\mathcal{F}^{-1}\left[\mathrm{e}^{i\varphi_0}\mathcal{F}(R_1(x)-iR_2(x))\right]\mathrm{e}^{i\omega x}\right\}\\
&=\mathcal{F}\left\{\left[R_1(x)-iR_2(x)\right]\mathrm{e}^{i(\omega x+\varphi_0)}\right\}\\
\tilde{S}_{+1}(k)=\tilde{O}(k)\bullet\tilde{H}(k+\omega)&=\mathcal{F}\left\{\mathcal{F}^{-1}\left[\tilde{O}(k-\omega)\bullet\tilde{H}(k)\right]\mathrm{e}^{-i\omega x}\right\}\\
&=\mathcal{F}\left\{\mathcal{F}^{-1}\left[\mathrm{e}^{-i\varphi_0}\mathcal{F}(R_1(x)+iR_2(x))\right]\mathrm{e}^{-i\omega x}\right\}\\
&=\mathcal{F}\left\{\left[R_1(x)+iR_2(x)\right]\mathrm{e}^{-i(\omega x+\varphi_0)}\right\}
\end{aligned}
$$

(24)

Eventually, the super-resolution image of the specimen can be obtained by adding the above two

first-order components to the zero-order component and inversely transforming the sum back to

real space:

$$
\begin{aligned}
I_{\text{SR-SIM}}(x)&=\mathcal{F}^{-1}\left\{\tilde{S}_0(k)+\tilde{S}_{+1}(k)+\tilde{S}_{-1}(k)\right\}\\
&=\mathcal{F}^{-1}\left\{\tilde{O}(k)\bullet\tilde{H}(k)+\frac{1}{2}\left[\tilde{O}(k)\bullet\tilde{H}(k+\omega)+\tilde{O}(k)\bullet\tilde{H}(k-\omega)\right]\right\}\\
&=\mathcal{F}^{-1}\left\{\mathcal{F}\left[R_0(x)\right]+\frac{1}{2}\mathcal{F}\left\{\left[R_1(x)+iR_2(x)\right]\mathrm{e}^{-i(\omega x+\varphi_0)}\right\}+\frac{1}{2}\mathcal{F}\left\{\left[R_1(x)-iR_2(x)\right]\mathrm{e}^{i(\omega x+\varphi_0)}\right\}\right\}\\
&=R_0(x)+R_1(x)\cos(\omega x+\varphi_0)+R_2(x)\sin(\omega x+\varphi_0)
\end{aligned}
$$

(25)

We can see that Eq. (20) and Eq. (25) are exactly the same. The former is deduced by the

reconstruction workflow in real space, while the latter is obtained by the conventional method

implemented in the Fourier domain. In the meantime, the intermediate formulae Eq. (22) and Eq.

(23) depict the relationship between the two reconstruction algorithms, which is the basis of the

JSFR-SIM.

To clarify the above relationships clearly, a relation diagram is presented in Fig. S7. For the spatial domain reconstruction algorithm, the super-resolved image without deconvolution can be obtained by multiplying the raw images with the pre-calculated coefficient functions and adding the products up, as shown in Eq. (5). In constrast, in the conventional reconstruction approach in the Fourier domain, the three spectrum components $\tilde{O}(k)\bullet\tilde{H}(k)$, $\tilde{O}(k\text{-}\omega)\bullet\tilde{H}(k)$, $\tilde{O}(k\text{+}\omega)\bullet\tilde{H}(k)$ are firstly separated by solving an inverse matrix equation. Afterwads, by shifting $\tilde{O}(k\text{-}\omega)\bullet\tilde{H}(k)$, $\tilde{O}(k\text{+}\omega)\bullet\tilde{H}(k)$ respectively to the right position and summing up all three components together, the super-resolved image without deconvolution can eventually be obtained by inverse Fourier transformation (Eq. (25)). Obviously, the workflow in Fourier domain is much more complex than that in real space.

In this note, to reveal the connection of above two algorithms, another workflow equivalent to the spatial domain reconstruction algorithm is exploited by rearranging the variables in the final super-resolultion image. First, nine intermediate images $R_0(x)$, $R_1(x)$, and $R_2(x)$ are obtained by recombining the raw images with specific scalar coefficients, as indicated by Eq.(19). By multiplying $R_0(x)$、$R_1(x)$、$R_2(x)$ respectively with 1, $\cos(\omega x+\varphi_0)$, $\sin(\omega x+\varphi_0)$ and adding the products together, we can also get the super-resolution image without deconvolution. It' worth noting that, in practical use, this workflow is more complex than that of the original algorithm in real space, as depicted in Eq.(5). Therefore, it can only be applied to demonstrate the relationship of the algorithms implemented in the Fourier domain and real space, however, is not suitable to be promoted as a new algorithm. The relationship of the two algorithms is manifested as the relation of the recombined raw images $R_0(x)$、$R_1(x)$、$R_2(x)$ and the frequency components $\tilde{O}(k)\bullet\tilde{H}(k)$, $\tilde{O}(k\text{-}\omega)\bullet\tilde{H}(k)$, $\tilde{O}(k\text{+}\omega)\bullet\tilde{H}(k)$, which can be converted to each other by Eq. (22)

and Eq.(23), as shown in Fig. S7d. Based on the relationship, the OTF compensation and the OTF attenuation approaches in the Fourier domain can be transferred into real space, providing a simple and rapid reconstruction protocol for thick specimens (Supplementary Note 2).

It should be noted that both reconstruction processes discussed here do not involve the deconvolution procedure. In conventional Wiener-SIM, the Wiener deconvolution is carried out by multiplying the spectrum components of the specimen with the pre-measured OTF before moving them to their true positions (also referred to as OTF compensation). However, in the SDR workflow, a routine Wiener deconvolution is instead employed by treating the above intermediate image as a new image acquired with a shrunken PSF, which is different from that of Wiener-SIM. In addition, for thick samples, to suppress the background fluorescence and periodic honeycomb artifacts, the OTF attenuation strategy is employed by attenuating the shifted spectrum components with an empirical Gaussian function, which was not included in the spatial domain reconstruction algorithm. In summary, the SDR reconstruction workflow differs from the conventional Wiener-SIM because of the absence of OTF compensation and OTF attenuation, which is prone to background fluorescence and honeycomb artifacts thereby limiting the resolution when imaging thick specimens (Fig. S1g).

Supplementary Note 2: Principle of JSFR-SIM

Based on the relationship of the two algorithms implemented in the Fourier and spatial domains, the SDR reconstruction workflow differs from the conventional Wiener-SIM because of the absence of OTF compensation and OTF attenuation. In this note, we prove the OTF compensation and OTF attenuation in the Fourier domain are equivalent to a preset notch filtering operation on the initial raw images. That is, these crucial procedures in conventional Wiener-SIM (OTF compensation and OTF attenuation) can be naturally and concisely applied to the reconstruction workflow in real space. On this basis, we developed a concise reconstruction workflow to rapidly obtain the optically sectioned, super-resolution image of a thick specimen by combining the spatial domain processing with the OS-SR-SIM implemented in the frequency domain, that is, the optically sectioned, super-resolution image of thick specimen can be rapidly attained by implementing the following procedures:

1) Estimate the parameters of illumination, including the wave vectors, the initial phases, and the modulation depth, and calculate the coefficient functions for each raw image with the estimated illumination parameters.

2) Calculate the reprocessed raw images by filtering the raw images $I_1(x)$、$I_2(x)$、$I_3(x)$ with a preset band-pass filter $\mathcal{F}^{-1}\left\{[1-a(\mathbf{k})] \cdot \tilde{H}^{*}(\mathbf{k})\right\}$.

3) Multiply the coefficient functions with the filtered raw images.

4) Sum the above results up and calculate the final image via Wiener filtering.

Considering this workflow combines the merits of both spatial domain reconstruction and the OS-SR-SIM implemented in the frequency domain, we, therefore, name it Joint Space and Frequency Reconstruction (JSFR-SIM).

On the contrary, the workflow of the conventional OS-SR-SIM algorithm in the frequency domain could be summarized as:

1) Estimate the parameters of illumination, including the wave vectors, the initial phases, and the modulation depth.

2) Transform all the raw images into the frequency domain.

3) Solve all the frequency components of the specimen with matrix equations.

4) Multiply these components with the sectioned OTF, and shift them back to the right position.

5) Sum all the sectioned spectra up and filter the expanded spectrum.

6) Calculate the final image by transforming the above spectrum back into the spatial domain.

2.1 Conventional Wiener-SIM algorithm implemented in Fourier domain

For 2D SR-SIM, the raw images are often acquired with nine sinusoidal excitation patterns with three equally spaced phase shifts in three orientations, which can be modeled as

$$
\begin{aligned}
D_{d,i}(\mathbf{r}) &= \left[O(\mathbf{r}) \cdot I(\mathbf{r})\right] \otimes H(\mathbf{r}) + B_{d,i}(\mathbf{r}) \\
&= \left\{O(\mathbf{r}) \cdot [1 + m_d \cos(\mathbf{k}_d \cdot \mathbf{r} + \varphi_{d,i})]\right\} \otimes H(\mathbf{r}) + B_{d,i}(\mathbf{r})
\end{aligned}
\tag{26}
$$

where $\mathbf{r}$ is the spatial domain coordinates, $O(\mathbf{r})$ denotes the distribution of the specimen, $I(\mathbf{r})$ represents the intensity distribution of the sinusoidal excitation patterns, m_d is modulation depth of the illumination pattern, $H(\mathbf{r})$ indicates the point spread function of the optical microscopy, $B_{d,i}(\mathbf{r})$ indicates the background in the raw image, $\mathbf{k}_d$ and $\varphi_{d,i}$ are respectively the wavenumber and the phase of the excitation pattern, the subscripts d (=1,2,3) and i (=1,2,3) respectively denote the index of the pattern orientation and the phase shifts.

To recover the SR image, the raw images are Fourier transformed to the frequency domain. Then, a set of linear equations which consists of the zero-order information component (lower frequency information) and $\pm 1^{st}$-order information components (higher frequency information) of the specimen can be constructed as follows[1]:

$$
\begin{bmatrix}
1 & m_d e^{i\varphi_{d,1}}/2 & m_d e^{-i\varphi_{d,1}}/2 \\
1 & m_d e^{i\varphi_{d,2}}/2 & m_d e^{-i\varphi_{d,2}}/2 \\
1 & m_d e^{i\varphi_{d,3}}/2 & m_d e^{-i\varphi_{d,3}}/2
\end{bmatrix}
\begin{bmatrix}
\tilde{O}(\mathbf{k})\tilde{H}(\mathbf{k}) \\
\tilde{O}(\mathbf{k}-\mathbf{k}_d)\tilde{H}(\mathbf{k}) \\
\tilde{O}(\mathbf{k}+\mathbf{k}_d)\tilde{H}(\mathbf{k})
\end{bmatrix}
+
\begin{bmatrix}
\tilde{B}_{d,1}(\mathbf{k}) \\
\tilde{B}_{d,2}(\mathbf{k}) \\
\tilde{B}_{d,3}(\mathbf{k})
\end{bmatrix}
=
\begin{bmatrix}
\tilde{D}_{d,1}(\mathbf{k}) \\
\tilde{D}_{d,2}(\mathbf{k}) \\
\tilde{D}_{d,3}(\mathbf{k})
\end{bmatrix}
\tag{27}
$$

where $\mathbf{k}$ denotes the frequency coordinates, $\tilde{D}_{d,i}(\mathbf{k})$ represents the raw images in the Fourier domain, and $\tilde{B}_{d,i}(\mathbf{k})$ is the spectrum of the background fluorescence in the raw images. Then the spectrum components can be separated with the equation set if the illumination pattern parameters $\mathbf{k}_d$, $\varphi_{d,i}$, m_d and the background information $\tilde{B}_{d,i}(\mathbf{k})$ are determined.

In situations where the background fluorescence is subtle, the background term in the Eq. (27) can be neglected. For instance, if the SIM setup works in total-internal-reflection (TIR) excitation mode, only the specimen within nearly 100 nm is excited, which results in neglectable background information in the raw images. Also, for thin and sparsely distributed specimens, little out-of-focus fluorescence will be collected by the camera.

Denoting the zero-order component and $\pm 1^{st}$-order components $\tilde{S}_{d,0}(\mathbf{k})$, $\tilde{S}_{d,\pm 1}(\mathbf{k})$ as following

$$
\begin{aligned}
\tilde{S}_{d,0}(\mathbf{k}) &= \tilde{O}(\mathbf{k})\tilde{H}(\mathbf{k}) \\
\tilde{S}_{d,+1}(\mathbf{k}) &= \tilde{O}(\mathbf{k})\tilde{H}(\mathbf{k}+\mathbf{k}_d) \\
\tilde{S}_{d,-1}(\mathbf{k}) &= \tilde{O}(\mathbf{k})\tilde{H}(\mathbf{k}-\mathbf{k}_d)
\end{aligned}
\tag{28}
$$

These components can be directly solved by

$$
\begin{bmatrix}
\tilde{S}_{d,0}(\mathbf{k}) \\
\tilde{S}_{d,+1}(\mathbf{k}-\mathbf{k}_d) \\
\tilde{S}_{d,-1}(\mathbf{k}+\mathbf{k}_d)
\end{bmatrix}
=
\begin{bmatrix}
1 & m_d e^{i\varphi_{d,1}}/2 & m_d e^{-i\varphi_{d,1}}/2 \\
1 & m_d e^{i\varphi_{d,2}}/2 & m_d e^{-i\varphi_{d,2}}/2 \\
1 & m_d e^{i\varphi_{d,3}}/2 & m_d e^{-i\varphi_{d,3}}/2
\end{bmatrix}^{-1}
\begin{bmatrix}
\tilde{D}_{d,1}(\mathbf{k}) \\
\tilde{D}_{d,2}(\mathbf{k}) \\
\tilde{D}_{d,3}(\mathbf{k})
\end{bmatrix}
\tag{29}
$$

Then, an expanded spectrum of the sample can be recovered by shifting higher frequencies to the correct position in frequency space. To get a nearly isotropic restoration of the SR image, the extended spectra at different orientations (0 °, 60 °, 120 °) can be combined as follows:

$$
\tilde{I}_{SR}(\mathbf{k}) = \sum_{d=1}^{3} \left[\tilde{S}_{d,0}(\mathbf{k}) + \tilde{S}_{d,+1}(\mathbf{k}) + \tilde{S}_{d,-1}(\mathbf{k}) \right]
\tag{30}
$$

To compensate for the modulation of the OTF on the images and improve the signal-to-noise ratio at peripheral regions of the spectrum, a Wiener-type filter is adopted as below:

$$
I_{\text{Wiener-OS-SR}}(\mathbf{k}) = \frac{\displaystyle\sum_{d=1}^{3} \tilde{S}_{d,0}(\mathbf{k})\tilde{H}^{*}(\mathbf{k}) + \tilde{S}_{d,+1}(\mathbf{k})\tilde{H}^{*}(\mathbf{k}+\mathbf{k}_d) + \tilde{S}_{d,-1}(\mathbf{k})\tilde{H}^{*}(\mathbf{k}-\mathbf{k}_d)}{\displaystyle\sum_{d=1}^{3} \left\{ \left|\tilde{H}(\mathbf{k})\right|^{2} + \left|\tilde{H}(\mathbf{k}+\mathbf{k}_d)\right|^{2} + \left|\tilde{H}(\mathbf{k}-\mathbf{k}_d)\right|^{2} \right\} + \alpha^{2}}
\tag{31}
$$

where each component is multiplied with the conjugate of the 2D OTF. This process is hereinafter termed OTF compensation. By summing these components up pointwise and dividing their sum by the sum of the squares of the OTFs plus a small constant, the final super-resolved image can be obtained. This workflow is frequently used in TIRF-SIM for the observation of thin samples.

However, as the majority of eukaryotic cells are at least several microns thick in the axial direction, the background information cannot be neglected. Consequently, the background term $\tilde{B}_{d,i}(\mathbf{k})$ in the left-hand of Eq. (27) should be treated as an additional term on the separated components.

Considering the 3×3 matrix in Eq. (27) is full-rank, $\tilde{B}_{d,i}(\mathbf{k})$ can be expressed as

$$\begin{bmatrix} 1 & m_d e^{i\varphi_{d,1}}/2 & m_d e^{-i\varphi_{d,1}}/2 \\ 1 & m_d e^{i\varphi_{d,2}}/2 & m_d e^{-i\varphi_{d,2}}/2 \\ 1 & m_d e^{i\varphi_{d,3}}/2 & m_d e^{-i\varphi_{d,3}}/2 \end{bmatrix} \begin{bmatrix} \tilde{b}_{d,0}(\mathbf{k}) \\ \tilde{b}_{d,+1}(\mathbf{k}) \\ \tilde{b}_{d,-1}(\mathbf{k}) \end{bmatrix} = \begin{bmatrix} \tilde{B}_{d,1}(\mathbf{k}) \\ \tilde{B}_{d,2}(\mathbf{k}) \\ \tilde{B}_{d,3}(\mathbf{k}) \end{bmatrix} \tag{32}$$

where $\tilde{b}_{d,0}(\mathbf{k})$ and $\tilde{b}_{d,\pm1}(\mathbf{k})$ are additional terms appended to the separated components. In the end, the spectrum components solved with Eq. (27) can be modified as

$$\begin{aligned} \tilde{S}_{d,0}(\mathbf{k}) &= \tilde{O}(\mathbf{k})\tilde{H}(\mathbf{k}) + \tilde{b}_{d,0}(\mathbf{k}) \\ \tilde{S}_{d,+1}(\mathbf{k}) &= \tilde{O}(\mathbf{k})\tilde{H}(\mathbf{k}+\mathbf{k}_d) + \tilde{b}_{d,+1}(\mathbf{k}+\mathbf{k}_d) \\ \tilde{S}_{d,-1}(\mathbf{k}) &= \tilde{O}(\mathbf{k})\tilde{H}(\mathbf{k}-\mathbf{k}_d) + \tilde{b}_{d,-1}(\mathbf{k}-\mathbf{k}_d) \end{aligned} \tag{33}$$

Considering the background mostly contributes to the low-frequency components, these additional terms will present a spectrum spike at the zero-position in frequency coordinates. Therefore, after moving these components to their proper position, the spectrum spike located at zero-position will also be moved to $\pm\mathbf{k}_d$, which results in six spectrum spikes (3×2) in the final spectrum, as shown in Fig. S1d. This is the source of the honeycomb artifacts induced by thick specimens (Fig. S1b).

In general, to restrain the out-of-focus background, the spectrum of the super-resolution image is typically obtained by removing the zero-order components of the specimen[15]:

$$\tilde{I}_{\text{OS-SR}}(\mathbf{k}) = \sum_{d=1}^{3} \left[\tilde{S}_{d,+1}(\mathbf{k}) + \tilde{S}_{d,-1}(\mathbf{k}) \right] \tag{34}$$

with which the background fluorescence contained in $\tilde{S}_{d,0}(\mathbf{k})$ is removed. However, it does not remove the out-of-focus information contained within the missing cones of the first order passbands, which is therefore helpless to eliminate the honeycomb artifacts in the final image.

To circumvent this problem, O'Holleran et al. proposed a linear reconstruction method that maximizes the axial frequency extent of the combined 2D structured illumination passband by attenuating the shifted spectrum components with the following equation[14]

$$\tilde{I}_{\text{OS-SR}}(\mathbf{k}) = \sum_{d=1}^{3} \left[a(\mathbf{k} + \mathbf{k}_d) + a(\mathbf{k} - \mathbf{k}_d) \right] \tilde{S}_{d,0}(\mathbf{k}) + [1 - a(\mathbf{k} + \mathbf{k}_d)] \tilde{S}_{d,+1}(\mathbf{k})$$
$$+ [1 - a(\mathbf{k} - \mathbf{k}_d)] \tilde{S}_{d,-1}(\mathbf{k})$$

(35)

where $\mathbf{k}$ denotes the 2-dimensional wave vector in the frequency domain, $\mathbf{k}_d$ represents the wave vector of the structured illumination in nth orientation. $a(\mathbf{k})$ is a Gaussian function, which is defined by

$$a(\mathbf{k}) = a_{\text{att}} e^{-\frac{\mathbf{k}^2}{2k_\sigma^2}}$$

(36)

in which the attenuation amplitude a_{att} and the attenuation width k_σ are empirically adjusted parameters.

However, in practice, we prefer the simpler attenuation function $1 - a(\mathbf{k})$ initially developed by Wicker et al[13] for the zero-order component, rather than the attenuation function $a(\mathbf{k} + \mathbf{k}_d) + a(\mathbf{k} - \mathbf{k}_d)$ designed by O'Holleran et al[14]. Similar to $a(\mathbf{k} + \mathbf{k}_d) + a(\mathbf{k} - \mathbf{k}_d)$, the simpler function $1 - a(\mathbf{k})$ also has a sunken region in the vicinity of zero, which therefore can effectively suppress the background information in the zero-order frequency component. Importantly, it reserves the useful middle- and high-frequency information in the zero-order component, which was mostly removed by the initial attenuation function $a(\mathbf{k} + \mathbf{k}_d) + a(\mathbf{k} - \mathbf{k}_d)$ but very useful and important to portray the true morphology of the specimen. For these reasons, the simpler function is more widely used to attenuate the zero-order component for OS-SR-SIM reconstructions, including the famous Fair-SIM[17] and the SR-OS-SIM code provided by Florian Ströhl (downloaded at the website: laser.ceb.cam.ac.uk). Also, a recent article about the high-fidelity reconstruction of SR-SIM[50] employed the identical attenuation function for the zero-order frequency component, whose explicit expression can be found in its supplementary notes. As such, Eq. (35) can be further simplified as

$$\tilde{I}_{\text{OS-SR}}(\mathbf{k}) = \sum_{d=1}^{3}\left[1 - a(\mathbf{k})\right]\tilde{S}_{d,0}(\mathbf{k}) + [1 - a(\mathbf{k} + \mathbf{k}_d)]\tilde{S}_{d,+1}(\mathbf{k})$$

$$+[1 - a(\mathbf{k} - \mathbf{k}_d)]\tilde{S}_{d,-1}(\mathbf{k}) \tag{37}$$

To flatten the frequency response of the optical transfer function (OTF) and noise, a Wiener filter is generally adopted by modifying the above equation as:

$$I_{\text{OS-SR}}(\mathbf{k}) = \frac{\sum_{d=1}^{3}\left\{\left[1 - a(\mathbf{k})\right]\tilde{S}_{d,0}(\mathbf{k})\tilde{H}^*(\mathbf{k}) + [1 - a(\mathbf{k} + \mathbf{k}_d)]\tilde{S}_{d,+1}(\mathbf{k})\tilde{H}^*(\mathbf{k} + \mathbf{k}_d) + [1 - a(\mathbf{k} - \mathbf{k}_d)]\tilde{S}_{d,-1}(\mathbf{k})\tilde{H}^*(\mathbf{k} - \mathbf{k}_d)\right\}}{\sum_{d=1}^{3}\left\{\left[1 - a(\mathbf{k})\right]\left|\tilde{H}(\mathbf{k})\right|^2 + [1 - a(\mathbf{k} + \mathbf{k}_d)]\left|\tilde{H}(\mathbf{k} + \mathbf{k}_d)\right|^2 + [1 - a(\mathbf{k} - \mathbf{k}_d)]\left|\tilde{H}(\mathbf{k} - \mathbf{k}_d)\right|^2\right\} + \alpha^2} \tag{38}$$

where α denotes the Wiener parameter. Also, other auxiliary processing tricks like apodization are usually adopted to improve the isotropy of the effective OTF.

2.2 JSFR-SIM algorithm based on spatial domain processing

In the SDR algorithm implemented in real space[23], the super-resolved image without deconvolution is directly attained by the superposition of the designed phase-shifted patterned illumination images $D_{d,i}(\mathbf{r})$ multiplied with each corresponding coefficient function $c_{d,i}(\mathbf{r})$, that is,

$$I_{\text{SR}}(\mathbf{r}) = \sum_{d=1}^{3}\sum_{i=1}^{3} c_{d,i}(\mathbf{r})D_{d,i}(\mathbf{r}) \tag{39}$$

where $c_{d,i}(\mathbf{r})$ are constant coefficient functions determined by the illumination parameters, including the modulation depth, the spatial frequency, the initial phase, and the phase shift. In the previous work[23], the phase shifts are limited to a specific value (0, 2π/3, 4π/3). This method is compatible with all possible phase shifts. By assuming the phase shifts is preset as $k_0\delta_i = \{0, \Delta\varphi, 2\Delta\varphi\}$, a general form of $c_{d,i}(\mathbf{r})$ could be derived as the following equations (see details in Supplementary Note 1)

$$c_{d,1}(\mathbf{r}) = \frac{1}{2(1-\cos\Delta\varphi)} + \frac{1-2\cos\Delta\varphi}{2(1-\cos\Delta\varphi)} m_d \cos(\mathbf{k}_d \cdot \mathbf{r} + \varphi_{d,0}) - \frac{2\cos\Delta\varphi+1}{2\sin\Delta\varphi} m_d \sin(\mathbf{k}_d \cdot \mathbf{r} + \varphi_{d,0})$$

$$c_{d,2}(\mathbf{r}) = -\frac{\cos\Delta\varphi}{1-\cos\Delta\varphi} + \frac{\cos\Delta\varphi}{1-\cos\Delta\varphi} m_d \cos(\mathbf{k}_d \cdot \mathbf{r} + \varphi_{d,0}) + \frac{1+\cos\Delta\varphi}{\sin\Delta\varphi} m_d \sin(\mathbf{k}_d \cdot \mathbf{r} + \varphi_{d,0}) \qquad (40)$$

$$c_{d,3}(\mathbf{r}) = \frac{1}{2(1-\cos\Delta\varphi)} - \frac{1}{2(1-\cos\Delta\varphi)} m_d \cos(\mathbf{k}_d \cdot \mathbf{r} + \varphi_{d,0}) - \frac{1}{2\sin\Delta\varphi} m_d \sin(\mathbf{k}_d \cdot \mathbf{r} + \varphi_{d,0})$$

where $\varphi_{d,0}$ is the initial phase of the pattern in the dth orientation. As such, the reconstruction algorithm implemented in real space can be extended to other commonly-used phase shifts, including $(0, \pi/2, \pi)$, $(0, 3\pi/5, 6\pi/5)$, and other possible values.

By rewriting the above coefficient functions in matrix form, the relationship of the spatial domain processing and frequency domain processing can be deduced (Supplementary Note 1). In brief, the relation of spatial domain images and frequency components can be concluded as

$$S_{d,0}(\mathbf{k}) = \mathcal{F}[R_{d,0}(\mathbf{r})]$$
$$S_{d,+1}(\mathbf{k}-\mathbf{k}_d) = e^{-i\varphi_{d,0}} \mathcal{F}[R_{d,1}(\mathbf{r}) + iR_{d,2}(\mathbf{r})] \qquad (41)$$
$$S_{d,-1}(\mathbf{k}+\mathbf{k}_d) = e^{i\varphi_{d,0}} \mathcal{F}[R_{d,1}(\mathbf{r}) - iR_{d,2}(\mathbf{r})]$$

where $R_{d,0}(\mathbf{r})$, $R_{d,1}(\mathbf{r})$, and $R_{d,2}(\mathbf{r})$ are linearly recombined raw images with specific coefficients extracted in the coefficient functions $c_{d,i}(\mathbf{r})$ (see Eqs. (16)-(19) in Supplementary Note 1).

Based on this relation, we find the result recovered in real space is equal to that of conventional reconstruction protocol without OTF compensation and OTF attenuation (see Supplementary Note 1 for details). In the frequency domain, these two tricks are implemented by multiplying an attenuated OTF $[1-a(\mathbf{k})]\tilde{H}^*(\mathbf{k})$ on the spectrum components, that is, the three spectrum components are respectively modulated as $[1-a(\mathbf{k})]\tilde{S}_{d,0}(\mathbf{k})\tilde{H}^*(\mathbf{k})$, $[1-a(\mathbf{k})]\tilde{S}_{d,+1}(\mathbf{k}-\mathbf{k}_d)\tilde{H}^*(\mathbf{k})$, and $[1-a(\mathbf{k})]\tilde{S}_{d,-1}(\mathbf{k}+\mathbf{k}_d)\tilde{H}^*(\mathbf{k})$, as shown in Eq.(38), before moving them to their proper positions. Apparently, the magnitude of illumination pattern-spatial

frequency $|\mathbf{k}_d|$ should be smaller than the cutoff frequency of the OTF to guarantee the effectiveness of the attenuation functions.

Therefore, based on the relationship in Eq. (41), we have

$$[1-a(\mathbf{k})]\bullet\tilde{H}^*(\mathbf{k})\bullet S_{d,0}(\mathbf{k}) = [1-a(\mathbf{k})]\bullet\tilde{H}^*(\mathbf{k})\bullet\mathcal{F}[R_{d,0}(\mathbf{r})]$$
$$[1-a(\mathbf{k})]\bullet\tilde{H}^*(\mathbf{k})\bullet S_{d,+1}(\mathbf{k}-\mathbf{k}_d) = [1-a(\mathbf{k})]\bullet\tilde{H}^*(\mathbf{k})\bullet e^{-i\varphi_{d,0}}\mathcal{F}[R_{d,1}(\mathbf{r})+iR_{d,2}(\mathbf{r})] \qquad (42)$$
$$[1-a(\mathbf{k})]\bullet\tilde{H}^*(\mathbf{k})\bullet S_{d,-1}(\mathbf{k}+\mathbf{k}_d) = [1-a(\mathbf{k})]\bullet\tilde{H}^*(\mathbf{k})\bullet e^{i\varphi_{d,0}}\mathcal{F}[R_{d,1}(\mathbf{r})-iR_{d,2}(\mathbf{r})]$$

Let us define three intermediate images $U_{d,0}(\mathbf{r})$, $U_{d,1}(\mathbf{r})$, and $U_{d,2}(\mathbf{r})$ as

$$U_{d,0}(\mathbf{r}) = R_{d,0}(\mathbf{r})\otimes\mathcal{F}^{-1}\left\{\left[1-a(\mathbf{k})\right]\tilde{H}^*(\mathbf{k})\right\}$$
$$U_{d,1}(\mathbf{r}) = R_{d,1}(\mathbf{r})\otimes\mathcal{F}^{-1}\left\{\left[1-a(\mathbf{k})\right]\tilde{H}^*(\mathbf{k})\right\} \qquad (43)$$
$$U_{d,2}(\mathbf{r}) = R_{d,2}(\mathbf{r})\otimes\mathcal{F}^{-1}\left\{\left[1-a(\mathbf{k})\right]\tilde{H}^*(\mathbf{k})\right\}$$

The above relation can be rewritten as

$$[1-a(\mathbf{k})]\bullet\tilde{H}^*(\mathbf{k})\bullet S_{d,0}(\mathbf{k}) = \mathcal{F}[U_{d,0}(\mathbf{x})]$$
$$[1-a(\mathbf{k})]\bullet\tilde{H}^*(\mathbf{k})\bullet S_{d,+1}(\mathbf{k}-\mathbf{k}_d) = e^{-i\varphi_{d,0}}\mathcal{F}[U_{d,1}(\mathbf{r})+iU_{d,2}(\mathbf{r})] \qquad (44)$$
$$[1-a(\mathbf{k})]\bullet\tilde{H}^*(\mathbf{k})\bullet S_{d,-1}(\mathbf{k}+\mathbf{k}_d) = e^{i\varphi_{d,0}}\mathcal{F}[U_{d,1}(\mathbf{r})-iU_{d,2}(\mathbf{r})]$$

which presents a high similarity with Eq. (41) if we consider the attenuated components at the left of Eq. (44) as three new spectrum components.

Considering that $R_1(x)$、 $R_2(x)$、 $R_3(x)$ is a linear superposition of the raw images, the filter operation in Eq. (43) can be directly transferred onto the raw images $D_{d,1}(\mathbf{r})$, $D_{d,2}(\mathbf{r})$, and $D_{d,3}(\mathbf{r})$:

$$D'_{d,1}(\mathbf{r}) = D_{d,1}(\mathbf{r})\otimes\mathcal{F}^{-1}\left\{[1-a(\mathbf{k})]\bullet\tilde{H}^*(\mathbf{k})\right\}$$
$$D'_{d,2}(\mathbf{r}) = D_{d,2}(\mathbf{r})\otimes\mathcal{F}^{-1}\left\{[1-a(\mathbf{k})]\bullet\tilde{H}^*(\mathbf{k})\right\} \qquad (45)$$
$$D'_{d,3}(\mathbf{r}) = D_{d,3}(\mathbf{r})\otimes\mathcal{F}^{-1}\left\{[1-a(\mathbf{k})]\bullet\tilde{H}^*(\mathbf{k})\right\}$$

By treating $D'_{d,1}(\mathbf{r})$, $D'_{d,2}(\mathbf{r})$, and $D'_{d,3}(\mathbf{r})$ as $D_{d,1}(\mathbf{r})$, $D_{d,2}(\mathbf{r})$, and $D_{d,3}(\mathbf{r})$, the processing can be implemented with the previous spatial domain reconstruction algorithm, that is, multiplying

the filtered raw images with corresponding coefficient functions and sum them up. The final super-resolution image is a superposition of the results of the three different pattern orientations.

Similarly, a Wiener filter can also be applied to the obtained OS-SR image by the following equation:

$$I_{\text{OS-SR}}(\mathbf{k}) = \mathcal{F}^{-1}\left\{\frac{\mathcal{F}[\sum_{d=1}^{3}\sum_{i=1}^{3} c_{d,i}(\mathbf{r})D'_{d,i}(\mathbf{r})]}{\sum_{d=1}^{3}\left\{[1-a(\mathbf{k})]\left|\tilde{H}(\mathbf{k})\right|^2 + [1-a(\mathbf{k}+\mathbf{k}_d)]\left|\tilde{H}(\mathbf{k}+\mathbf{k}_d)\right|^2 + [1-a(\mathbf{k}-\mathbf{k}_d)]\left|\tilde{H}(\mathbf{k}-\mathbf{k}_d)\right|^2\right\} + \alpha^2}\right\} \quad (46)$$

It's worth noting that selecting appropriate parameters of the attenuation function is very important for a successful reconstruction. As demonstrated above, the empirical parameters a_{att} and k_σ in the attenuation function here are inherited from the conventional Wiener-SIM. Therefore, the adjustment of these two parameters is in principle identical to that of the conventional Wiener-SIM. Thereinto, the attenuation amplitude a_{att} is generally employed to adjust the optical sectioning performance of OS-SR-SIM, which ranges from 0 to 1, depending on the background level in the raw data. For thin specimen or TIRF-SIM results with subtle background, a_{att} is generally set to zero to turn off the OTF attenuation. For raw data with strong background fluorescence, it is usually set to 0.9~1 to effectively suppress the background information. Also, the width of the Gaussian function k_σ is designed to adjust the area of the attenuation function. An excessively low value of k_σ will result in abundant residual backgrounds in the SR image. On the contrary, an excessively high value will remove most of the low-frequency information of the specimen and decrease the signal-to-noise ratio of the final SR image. In most cases, the attenuation width of 1.0~2.0 cycles/micron is acceptable and we set it as 1.5 cycles/micron by default.

In this note, we demonstrate that the OTF compensation and OTF attenuation in Wiener-SIM equals preset filtering operations on the raw images. Thereinto, the former equals a low-

pass filter $H^*(\mathbf{k})$, while the latter is identical to a high-pass filter $[1-a(\mathbf{k})]$. In addition, the OTF compensation and OTF attenuation can easily be cooperated to a new filter $H^*(\mathbf{k})[1-a(\mathbf{k})]$. The selection of the high-pass filter $[1-a(\mathbf{k})]$ to suppress the out-of-focus background is somewhat intuitive and empirical. It was derived from the OTF attenuation method in conventional Wiener-SIM, which was empirically designed to attenuate the additional background term in the separated spectrums (see Section 2.1 of the Supplementary Notes). Although it eventually becomes a high-pass filter on the raw images in the JSFR method, it's not the straightforward application of the general high-pass filtering. Therefore, the concept to suppress the low-frequency background of the JSFR method has some similarity to conventional optical sectioning structured illumination microscopy based on spectrum filtering like the HiLo method[51], but the concrete procedures and the source of ideas are different.

Supplementary Note 3: Resolution enhancement of the JSFR-SIM

To calibrate the spatial resolution of JSFR-SIM, we tested sparsely distributed fluorescent beads with a diameter of 40 nm (505/515, Thermo Fisher Scientific Inc., USA) and recovered the separate Wiener-SIM and the JSFR-SIM OS-SR-SIM images (Fig. 3). The adjacent two beads which are unable to be resolved in the widefield image are separated in the JSFR-SIM and Wiener-SIM images (Fig. 3b). To qualify the spatial resolution, 30 isolated fluorescent beads are selected and their full width at half maximum (FWHM) along the x- and z-axes are measured and counted. The averaged FWHM values in xy dimensions for wide-field, JSFR-SIM, and Wiener-SIM are measured as 232±12 nm, 108±5 nm, and 111±6 nm, respectively. Thus, the lateral resolution of both JSFR-SIM and Wiener-SIM show an improvement of ~115% relative to wide-field microscopy. Further, the averaged FWHM values along the z-axis are 626±14 nm, 643±13 nm, and 649±16 nm, respectively. Although the JSFR-SIM and Wiener-SIM cannot improve the axial resolution, the out-of-focus background is significantly reduced, as exhibited by the xz cross-sectioned images of the isolated bead in Fig. 3c.

In addition, we also compared their resolution performance by analyzing the reconstruction results of a commercially available standard specimen, Argo-SIM (Fig. S4). The pattern E in Argo-SIM is "gradually spaced lines pairs" patterns in which the distance between the lines pairs gradually increases from 0 to 390 nm with a step of 30 nm. For the widefield microscope, the eighth line pair is too vague to be discerned, indicating the resolution of the widefield microscope is less than 210 nm. As a comparison, in the SR image recovered by the custom-developed Wiener-SIM, JSFR-SIM, and the open-source Fiji plugin FairSIM, the fifth line pairs can be distinguished, indicating the resolution achieved by these algorithms is higher than 120nm.

This result is consistent with the measurement results of fluorescent beads. The intensity profiles

in Fig. S4j provided a more distinct comparison of the resolution performance of each algorithm.

Supplementary Note 4: Details of sample preparations

Fluorescent, 40 nm diameter beads and the commercial Argo-SIM slide were employed as standard specimens to evaluate the performance of JSFR-SIM. The carboxylate-modified fluospheres (yellow-green fluorescent 505/515, F8795, Thermo Fisher Scientific Inc, USA) were first diluted 200 times and dispensed onto the coverslip. The suspension on the coverslip was dried in air for 3 h, and then covered by a drop (3 μL) of Prolong Gold reagent (No. P36934, ThermoFisher Inc., USA). The refractive index of Prolong Gold is 1.526, which is close to the refractive index of the mounting medium (1.515) for the oil-immersion objective lens, reducing the spherical aberration caused by refractive-index-mismatch.

COS-7 cells were purchased from American Type Culture Collection (ATCC). Cells were cultured in high-glucose DMEM supplemented with 10% FBS and 1% 100 mM sodium pyruvate solution (Sigma-Aldrich, S8636) and grown under standard cell culture conditions (5% CO_2, humidified atmosphere at 37 ℃). Prior to imaging, cells were plated on DMEM/Ham's F-12 pre-incubated glass coverslips for 24 h. For cell passage, cells were washed with PBS (Life Technologies, #14190500BT) and digested with trypsin (Gibco, #25200-056). All cell lines were routinely tested for potential mycoplasma contamination (MycoAlert, Lonza) and all tests were negative. To label mitochondria, cells were incubated with 500 nM PK Mito Deep Red[52] in DMEM at 37 ℃ for 30 min and washed with PBS 3 times. To label microtubules and cargo, COS-7 cells were transfected with 4μg MAP4-GFP. Experiments were conducted 24 h after DNA transfection.

The DNA was transfected into the cells using a 2D Nucleofector Device (Lonza). On the day of electroporation, trypsinized cells were transiently transfected with an electroporation cup (BIORAD, #165-2086) using program W-001 for COS-7 cells. The electroporation buffer

contains solution I and solution II. Solution I contains 2 g ATP-disodium salt (Sigma Aldrich, A2383), 1.2 g $MgCl_2$-$6H_2O$ (Sigma Aldrich, M2393), with ddH_2O up to 10 ml; Solution II contains 6 g KH_2PO4 (Sigma Aldrich, P5655), 0.6 g $NaHCO_3$ (Sigma Aldrich, S-5761), 0.2 g glucose (Sigma Aldrich, G-6152), adjust pH to 7.4, and add ddH_2O to 500 ml. After filter sterilization (0.22 μm), 80 μl Solution I was mixed with 4 ml Solution II and stored at 4 ℃ for up to one month. Experiments were conducted 24 h after DNA transfection.
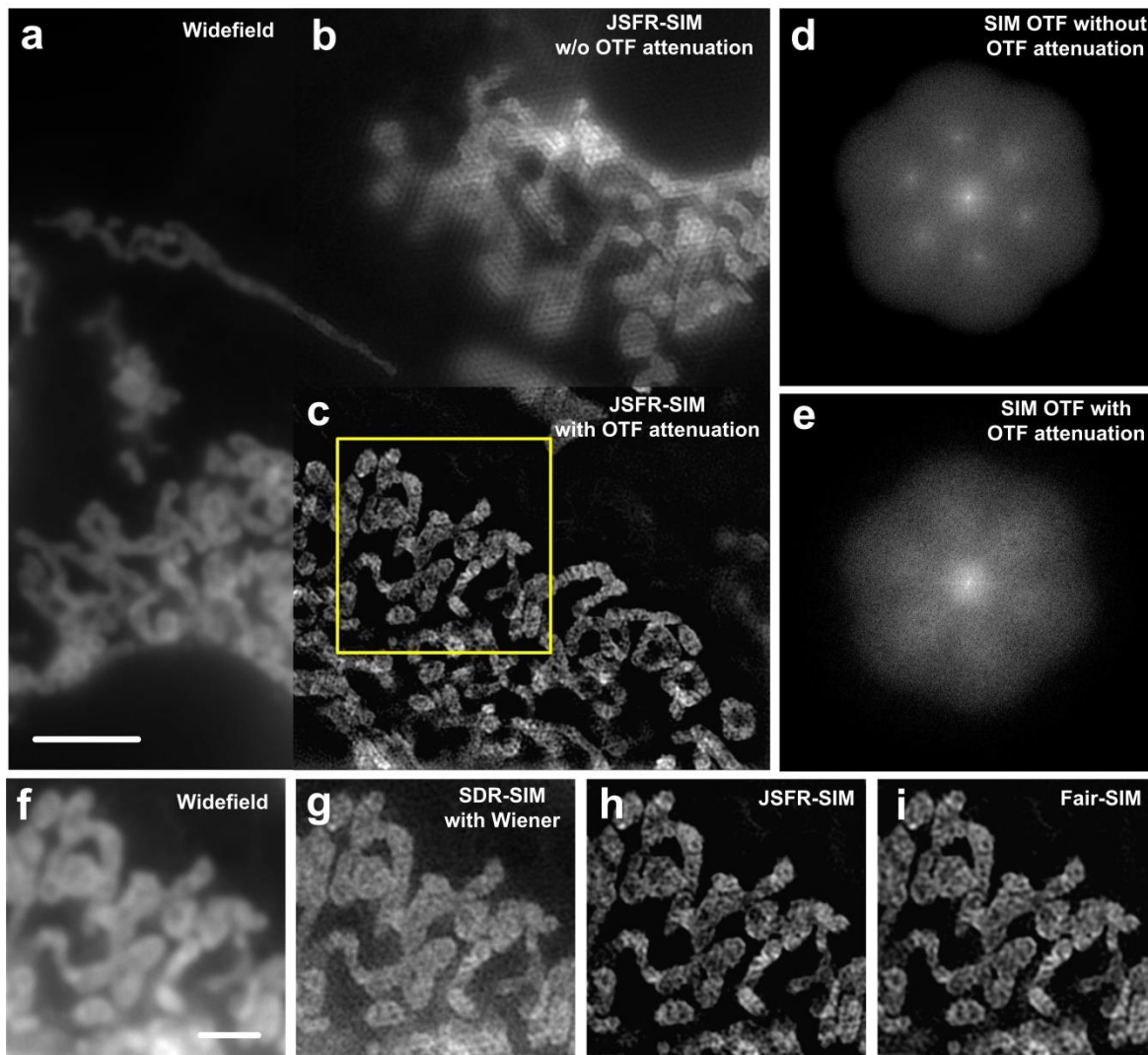
Supplementary Figures:

Fig. S1 JSFR-SIM with OTF attenuation significantly suppresses both background fluorescence and honeycomb artifacts. (a) The wide-field image of mitochondria in COS7 cells. (b) The SIM image recovered using the Wiener-SIM algorithm without using OTF attenuation. (c) The SIM image reconstructed using the Wiener-SIM algorithm with OTF attenuation. (d) The enlarged spectrum in (b). (e) The enlarged spectrum in (c). (f) The widefield image of the yellow-boxed region in (c). (g) The SR image reconstructed using SDR. (g) The SR-OS image reconstructed using the JSFR-SIM algorithm with both OTF compensation and OTF attenuation. (h) The OS-SR image reconstructed using the Fair-SIM plugin for ImageJ which incorporates OTF attenuation. Scale bars: (a)-(c) 5 μm; (f)-(i) 2 μm.
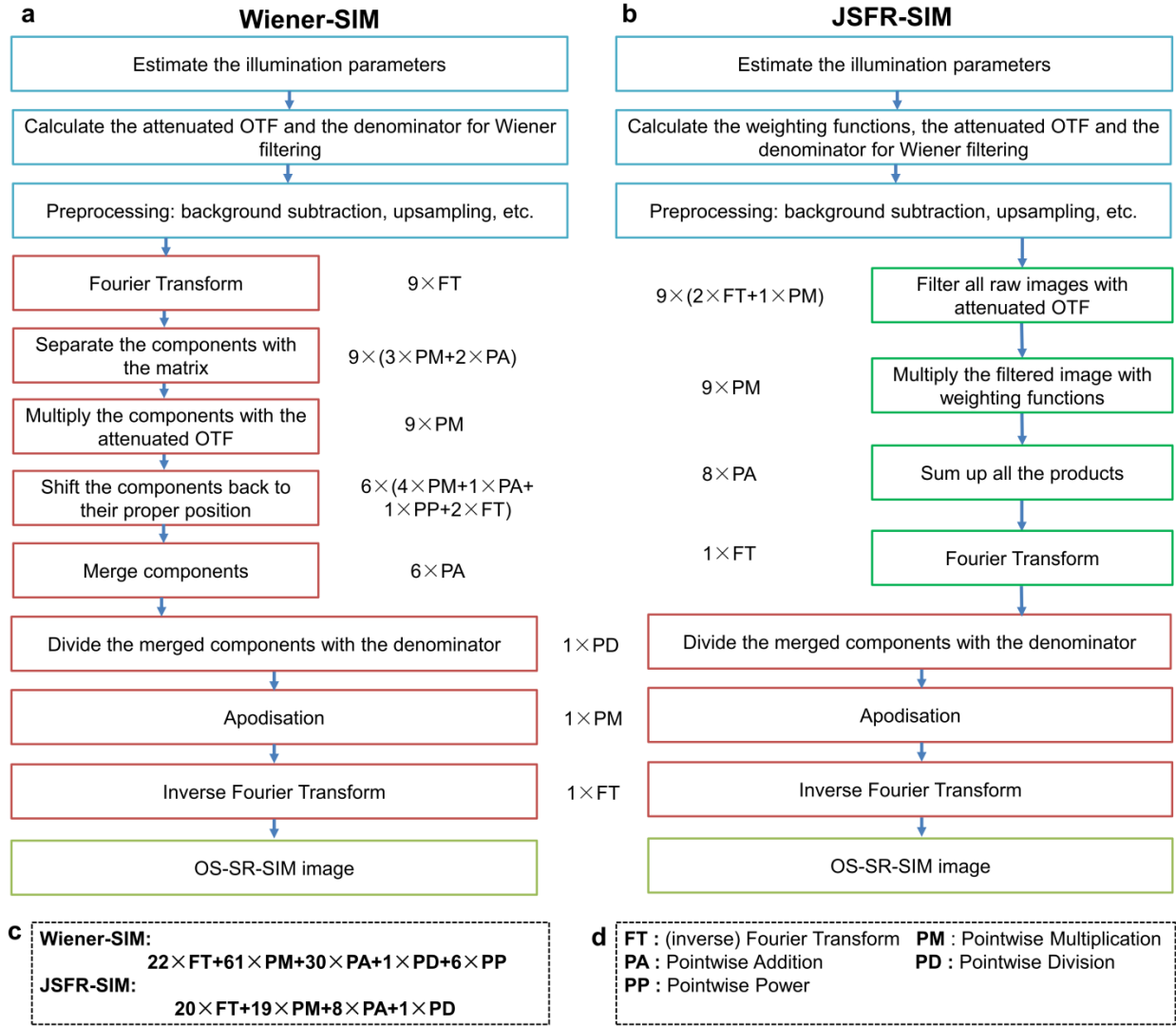
a **Wiener-SIM**

Estimate the illumination parameters	
Calculate the attenuated OTF and the denominator for Wiener filtering	
Preprocessing: background subtraction, upsampling, etc.	
Fourier Transform	$9\times$FT
Separate the components with the matrix	$9\times(3\times$PM$+2\times$PA$)$
Multiply the components with the attenuated OTF	$9\times$PM
Shift the components back to their proper position	$6\times(4\times$PM$+1\times$PA$+1\times$PP$+2\times$FT$)$
Merge components	$6\times$PA
Divide the merged components with the denominator	$1\times$PD
Apodisation	$1\times$PM
Inverse Fourier Transform	$1\times$FT
OS-SR-SIM image	

b **JSFR-SIM**

Estimate the illumination parameters	
Calculate the weighting functions, the attenuated OTF and the denominator for Wiener filtering	
Preprocessing: background subtraction, upsampling, etc.	
$9\times(2\times$FT$+1\times$PM$)$	Filter all raw images with attenuated OTF
$9\times$PM	Multiply the filtered image with weighting functions
$8\times$PA	Sum up all the products
$1\times$FT	Fourier Transform
Divide the merged components with the denominator	
Apodisation	
Inverse Fourier Transform	
OS-SR-SIM image	

c

Wiener-SIM:
$22\times$FT$+61\times$PM$+30\times$PA$+1\times$PD$+6\times$PP

JSFR-SIM:
$20\times$FT$+19\times$PM$+8\times$PA$+1\times$PD

d

FT : (inverse) Fourier Transform   PM : Pointwise Multiplication
PA : Pointwise Addition   PD : Pointwise Division
PP : Pointwise Power

Fig. S2 Comparison of the workflow of Wiener-SIM and JSFR-SIM. (a) The workflow of Wiener-SIM. (b) The workflow of JSFR-SIM. (c) Comparison of the computing burden of Wiener-SIM and JSFR-SIM. (d) Definition of the symbols in panels a-c.
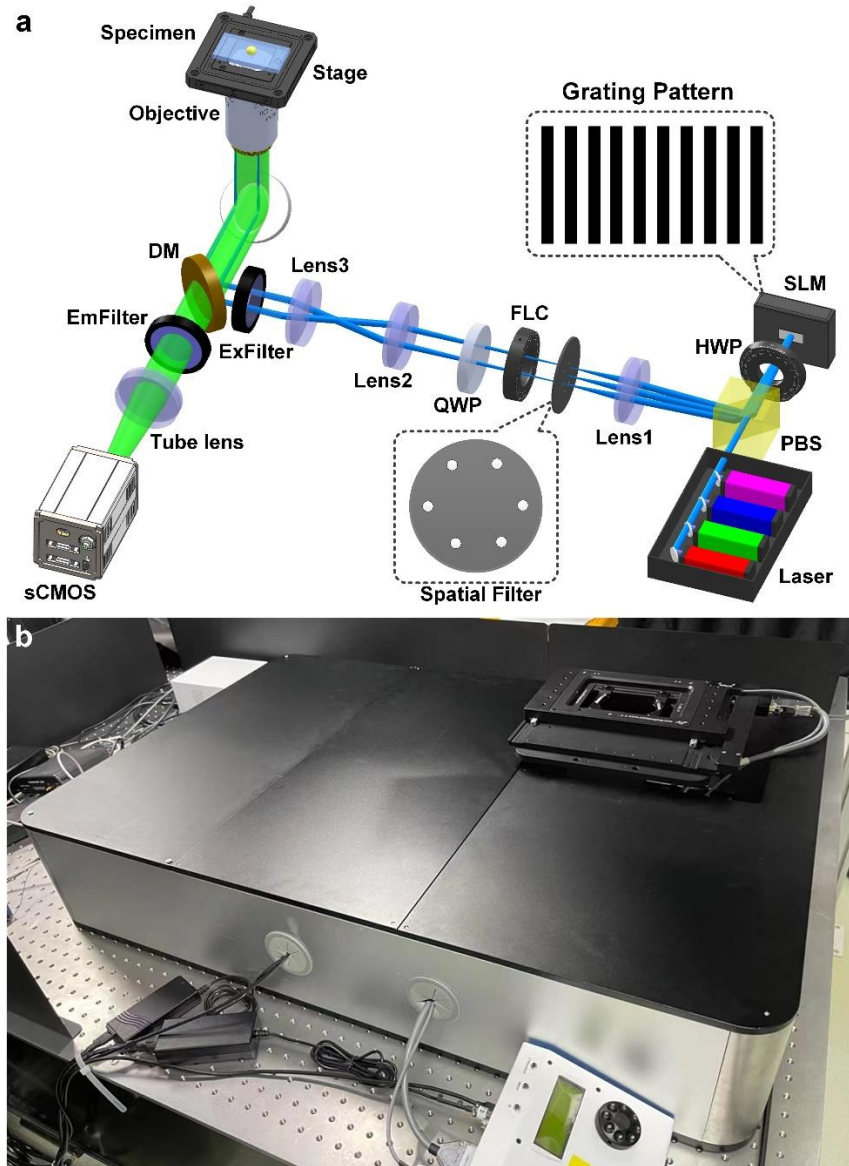
Fig. S3 Layout of the custom-built SR-SIM setup. (a) Schematic of the SR-SIM system. The incident laser beam is first diffracted into various orders after being modulated by the SLM. Afterward, the ±1-orders diffraction orders are selected with a spatial filter. These two coherent beams are then converted to circular polarization and relayed onto the back focal plane of the microscope objective, producing sinusoidal patterns on the specimen. Shift and rotation of the illumination field are achieved by changing the binary patterns on the SLM. PBS: polarized beam splitter; SLM: spatial light modulator; FLC: ferroelectric liquid crystal phase retarders; HWP: half-wave plate; QWP: quarter-wave plate; ExFilter: excitation filter; EmFilter: emission filter; DM: dichroic mirror. (b) A photograph of the custom-built SR-SIM steup.
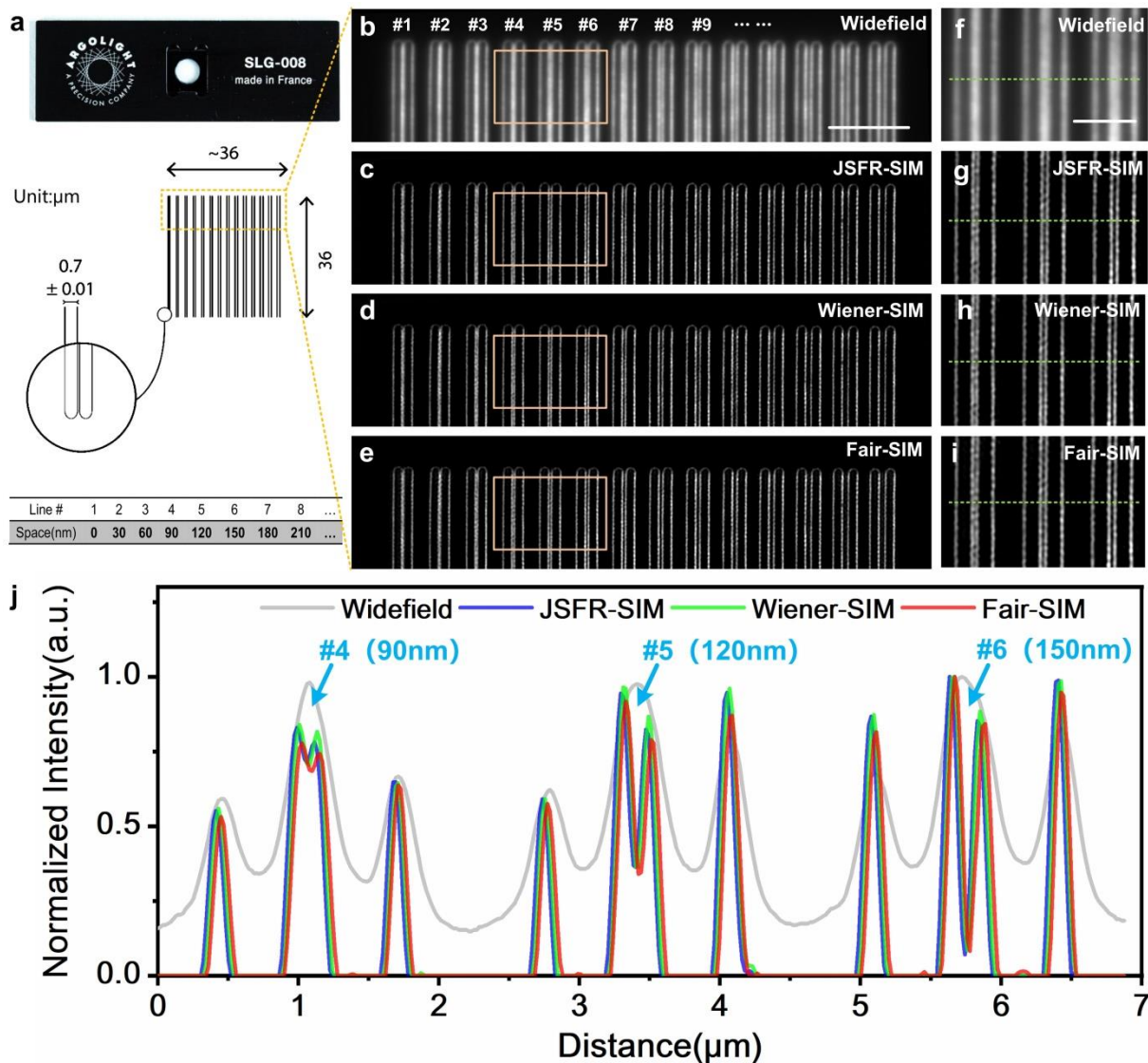
Fig. S4 The lateral resolution of the SIM reconstruction algorithms is comparable. (a) The Argo-SIM slide used to assess resolution. Pattern E of the slide consists of 36 μm-long lines spaced increasingly further apart using a step size of 30 nm. (b) The wide-field image of the lines. (c)-(e) are OS-SR-SIM images of the lines recovered with Wiener-SIM, JSFR-SIM, and Fair-SIM plugin, respectively. (f)-(i) are the close-up views of the widefield and SR-SIM images recovered with Wiener-SIM, JSFR-SIM, and Fair-SIM plugin, as indicated by the yellow-boxed region in (a). Panel (j) is the intensity profiles of the images along the green dashed lines in (f)-(i). The negative intensity values in the reconstructed images are truncated at the last step of JSFR-SIM and Wiener-SIM. Scale bars: (b)-(e) 5 μm; (f)-(i) 2 μm.
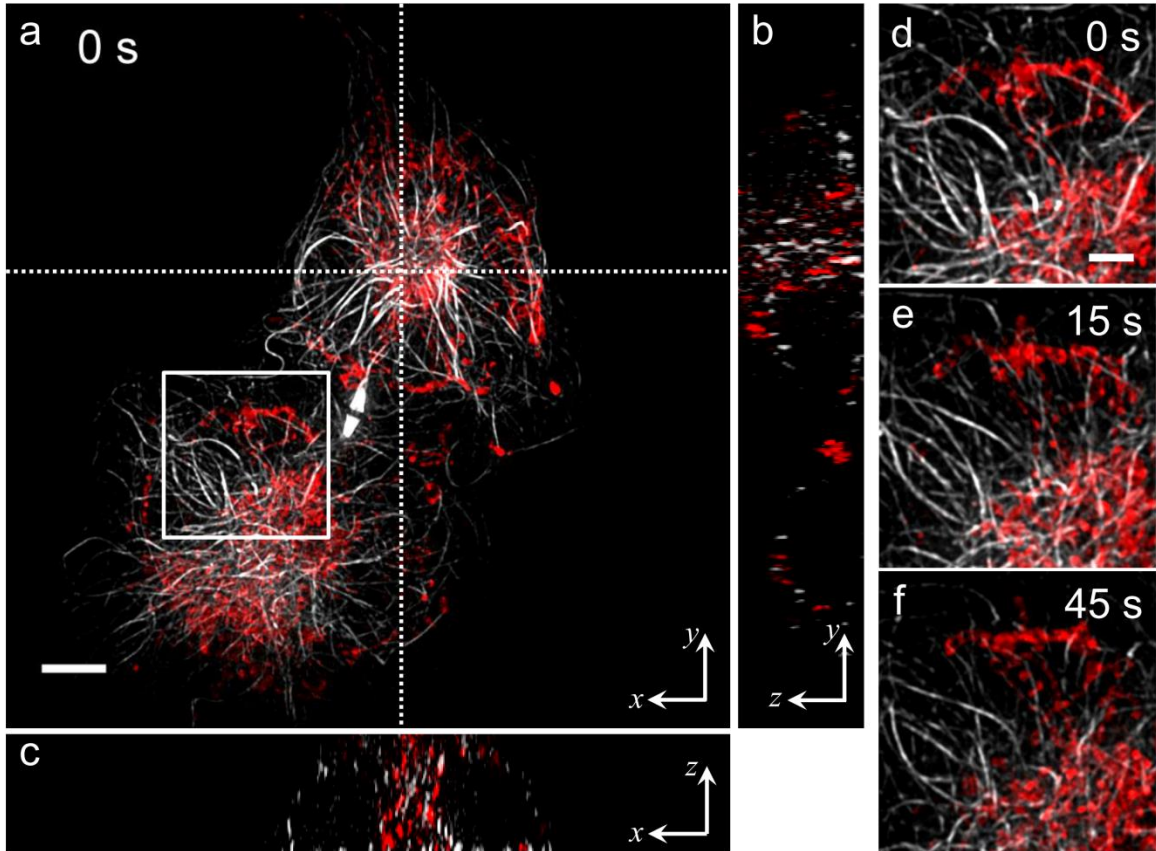
Fig. S5 JSFR-SIM enables dual-color, 3D, dynamic observation of thick COS-7 cells (Video 2). Microtubules (gray) and mitochondria (red) of the COS-7 cells are respectively stained with sfGFP and MitoTracker Red. Each 3D image is obtained by scanning the focal plane of the system through the cells with a scanning interval of 300 nm and scanning planes of 30. The time series consists of ten 3D volumes at a time interval of 15 seconds. (a) The maximum-intensity-projection image of the cell along the z-axis at the time t=0, in which the microtubules and the mitochondria are respectively rendered in gray and red. (b) The *yz* cross-section image of the volume t=0 along the vertical dashed line in (a). (c) The *xz* cross-section of the volume t=0 along the horizontal dashed line in (a). (d)-(f) are the maximum-intensity-projection images of the cells at three of the ten time-points, focused on the white-boxed region in panel (a). Scale bars: (a) 5 μm; (d)-(e) 2 μm.
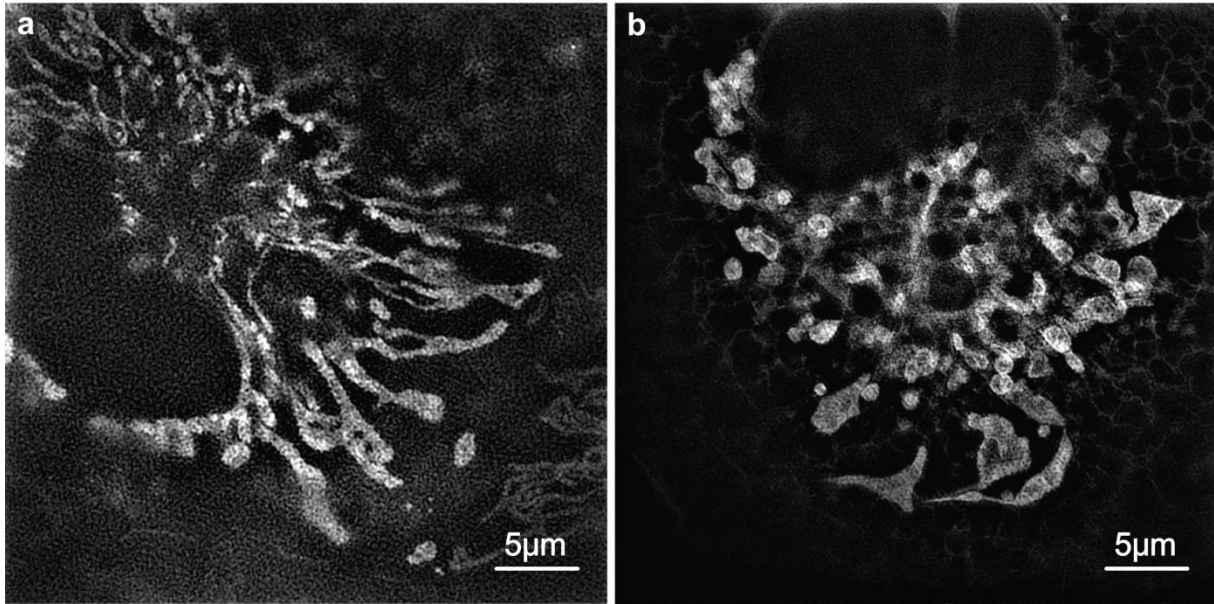
Fig. S6 Real-time observation enables the observer to fast skip undesirable FOVs which contain limited numbers of healthy mitochondria. (a) Unhealthy mitochondria with thin filaments are not well stained with mitochondria-specific dye. (b) Swollen mitochondria after long-term, high-power exposure. The extended exposure time damages the mitochondria, resulting in poor imaging.
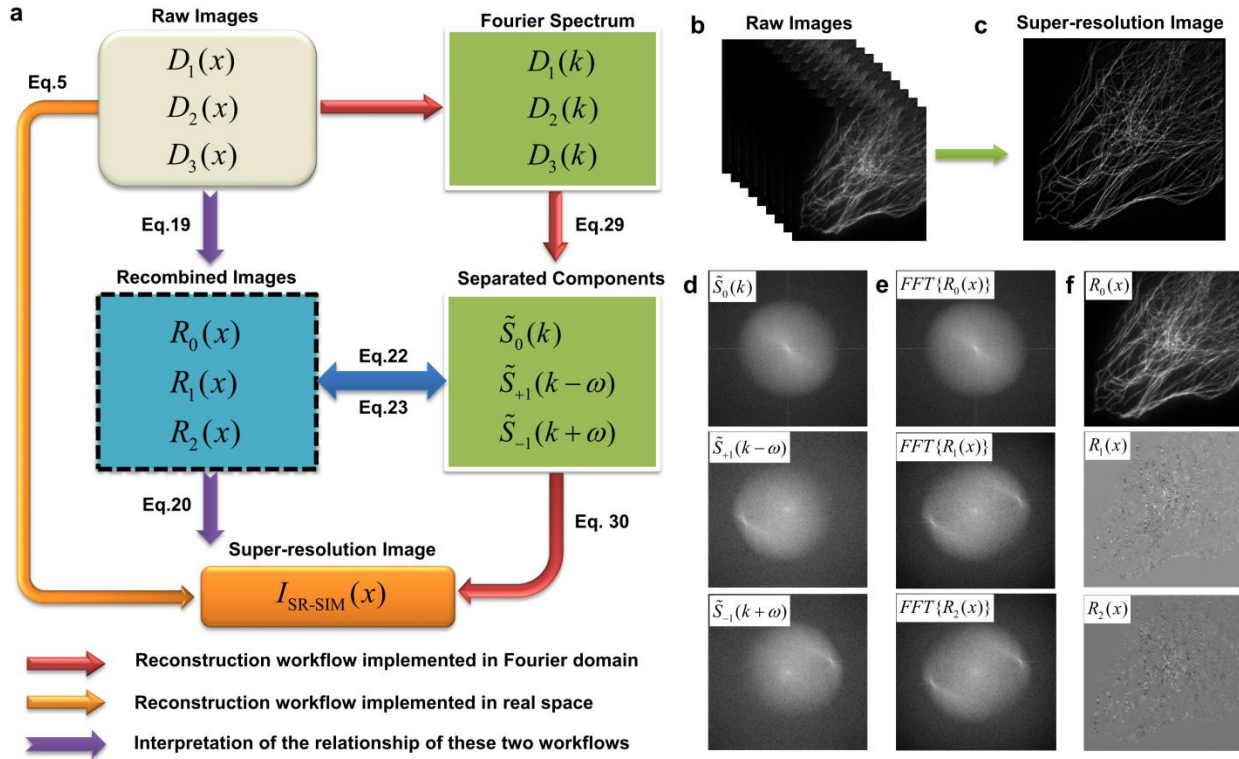
Fig. S7 Diagrams to clarify the relationship of the reconstruction workflows in the Fourier domain and real space. (a) The relation diagram of the three workflows, including the reconstruction workflow implemented in the Fourier domain (green); the reconstruction workflow implemented in real space (orange); and the derived reconstruction workflow (blue) in real space. (b) Raw sample, SIM images. (c) A super-resolution image reconstructed with the raw images in (b). (d) The three spectrum components are separated from the raw images of single pattern orientation in Fourier domain processing. Spectra in panel (e) are the Fourier transform of the three recombined images of (f) in real space. The mathematical relation of (d) and (e)-(f) was described by Eqs. (22)-(23) in Supplementary Note 1.